96 - 101

PERFORMANCE
OF THE TGT LIQUID ARGON CALORIMETER
AND TRIGGER SYSTEM
## RD33 Collaboration

1996

1 Introduction

The novel TGT (Thin Gap Turbine) concept for electromagnetic liquid argon calorimetry has been developed in the framework of the R&D project RD33 [1], which is part of the overall R&D programme for experimentation at the LHC of CERN. In our recent paper [2] concerning phase I of the project we have shown that the TGT structure can be realized and that the calorimeter behaves (w.r.t. energy- and angular resolution as well as homogeneity) as expected from Monte Carlo simulations. It is well suited for applications in experiments at high luminosity hadron colliders like the LHC.

This paper deals with phase II of the project (as announced in [2]) emphasizing the TGT-adapted readout electronics and the trigger system. The front-end electronics is located in the cold, where especially the preamplifiers (in gallium-arsenide technology) have been mounted very close to the signal electrodes: they are integrated into the multilayer boards which are directly attached to the absorber elements. The summing and shaping amplifiers with a peaking time of 45 ns are also operated in the cold thus minimizing the number of feedthroughs. For the trigger studies a FADC system with readable memory was built and operated in connection with a level-1 trigger processor developed by the RD27 collaboration [3], [4].

The paper is organized in the following way: First, we describe the relevant features of the calorimeter structure and of the amplifier electronics. Then we discuss first results on the behaviour of the calorimeter: response to electrons and muons, energy- and angular resolution. Finally, the trigger electronics and the performance of the trigger system (efficiency, timing accuracy, energy resolution) are presented.

2 The Calorimeter Structure

The TGT test calorimeter is assembled out of 36 independent identical flat absorber elements (ABE's) geometrically arranged as shown in Fig. 1. Mounted in the barrel part of a collider detector, any particle produced at the interaction point would cross the individual absorber elements under a fixed angle of about 45°. Each ABE consists of four absorber plates, three double gaps of 2 × 0.8 mm LAr with readout electrodes ('padboards') in the centre, and at the end a multilayer board which carries preamplifier chips and calibration
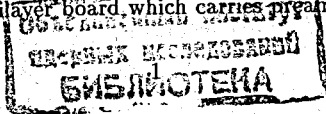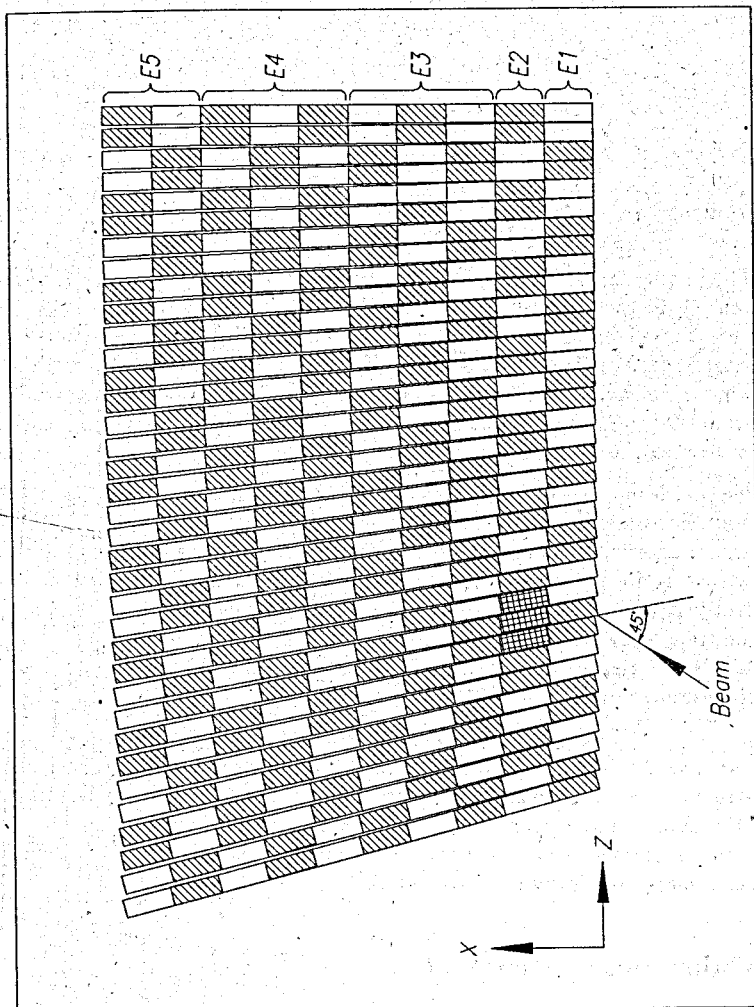
Figure 1: Schematic view of the TGT calorimeter module. The longitudinal summation is indicated by the symbols E. The cross-hatched absorber elements are equipped with strips.

capacitors (thickness of the board ~ 1.5 mm, total thickness including the electronic chips ~ 3.5 mm). The two inner absorber plates are made of 1.65 mm lead and the two outer plates consist of 2.0 mm stainless steel, the thickness of which has been chosen to maintain a constant sampling fraction. The area of an ABE is 425×364 mm^2 with a geometrical thickness of 18.4 mm. The total depth of the test calorimeter amounts to 21.5 radiation lengths (X_0).

Table 1: Parameters for one readout cell.

Argon gap width	6×0.8 mm
Padsize	42.5×30 mm^2
Spacing between pads	0.3 mm
Detector capacity	$120 pF/3$ double gaps
HV decoupling capacity	$4800 pF/3$ double gaps
Dead area	$\leq 1\%$
Thickness	$0.89 X_0$
Geometrical thickness	18.4 mm
Molière radius	2.15 cm
Sampling fraction	6.2%

Originally it was planned to clad the lead plates with 0.1 mm stainless steel foils. For reasons given in [2] the phase I measurements were done with bare lead plates. Probably due to small metal whiskers lifting up from the lead surface during cool down, high voltage problems occured in some of the gaps. In order to improve on this for the phase II measurements, we decided to coat the lead plates with nickel (thickness $\sim 30\mu m$). This resulted in a very satisfactory behaviour during a test cooldown of the whole calorimeter with liquid nitrogen. Only one gap out of 216 showed an enlarged current. However, in spite of very careful handling and testing during the final installation into the cryostat at the CERN test beam, even more gaps than in phase I developed shorts during cooldown. In total, 9 out of 216 gaps drew such high currents that their high voltage had to be switched off. This required correction procedures at the analysis stage which are described below.

The 120 pads (10×12) of each padboard have an identical size of 42.5×30 mm^2, separated by 0.3 mm. Viewed under the incident angle of 45° their shape appears quadratic (30×30 mm^2) corresponding to a minimal angular granularity in pseudorapidity and azimuth of $\Delta\eta \times \Delta\varphi = 0.02 \times 0.02$, calculated for a barrel calorimeter of a collider detector at a radial distance of 1.5 m from the interaction point. The corresponding pads of the three consecutive double gaps in the ABE's are electrically connected in parallel to each other and to the multilayer board on which the preamplifier channel is mounted; this constitutes the basic readout cell. The electrical field in the LAr gap is generated by connecting the coating of high electrical resistivity ($1 M\Omega/\square$) on the pad boards to high voltage (typically 800 volt).

In three absorber elements an area of two pads is divided into strips. Their location at a depth of $2.5 - 5 X_0$ is indicated in Fig. 1. In total, there are eight vertical strips with a spacing of about 5 mm and 16 horizontal strips with a spacing of about 3.8 mm. Details on mechanical construction, tolerances and the padboard design can be found in [2]. For

convenience, some relevant parameters for one readout cell are given in Tab. 1.

3   The Electronic Readout Structure

The concept is based on the notion of 'active pads', i.e. a separate preamplifier for each pad with active summation of pads in subsequent readout planes. These sums constitute the readout channels as read by the data acquisition system. The summation is indicated in Fig. 1. These summed signals form the longitudinal readout structure. The signals are shaped and filtered in the LAr and are readout via cold to warm feedthroughs. In the following, we will specify the requirements for the electronics operation in the LHC environment and from the physics point of view.

3.1   Requirements

The environment in which the electronics has to be operated is characterized by high pile-up rates and radiation levels. A neutron fluence of $\sim 10^{15}$ n/cm^2 and a photonic dose of 10 Mrad are typically accumulated over a period of ten years.

From the point of view of the energy resolution of electrons, preamplifiers entering in one summing channel should have the same gain within $\pm 3\%$, and a linearity in both the high and the low signal range of better than $\sim 1\%$, the accuracy of the calibration system should be better than $\sim 0.5\%$, and the timing accuracy better than 1 ns. The dynamic range is such that the maximum energy is assumed to come from 2 TeV electrons, and the signal of single muons should be detectable.

It is expected that the maximal energy deposit in one readout cell is in the cells 6 to 8 from the front. At LHC it will be $\sim 40,000$ times higher than the energy deposited by a minimum ionizing particle. In the summed readout sections 2, 6 or 8 gaps are grouped into one channel and here the maximum will be $\sim 30,000$ times higher than the MIP signal. Consequently, the digital readout system will need a dynamic range of 14-bits for operation at LHC energies.

The operation of a large number of amplifier channels in the liquid argon puts an upper limit on the power consumption of about 20 mW/channel.

3.2   Concept and Design

The conceptual design of the front-end electronics is shown in Fig. 2. The system is located in the liquid argon on the back of the individual absorber elements, the calibration input being at the amplifier level. The signal shapers are located on the backside of the calorimeter module in the liquid argon, while the calibration pulsers are located outside of the cryostat in the warm.

The key elements of the amplifier system are a chip integrating eight preamplifier channels, and a chip integrating two channels each consisting of a summing (8 channels) and shaping
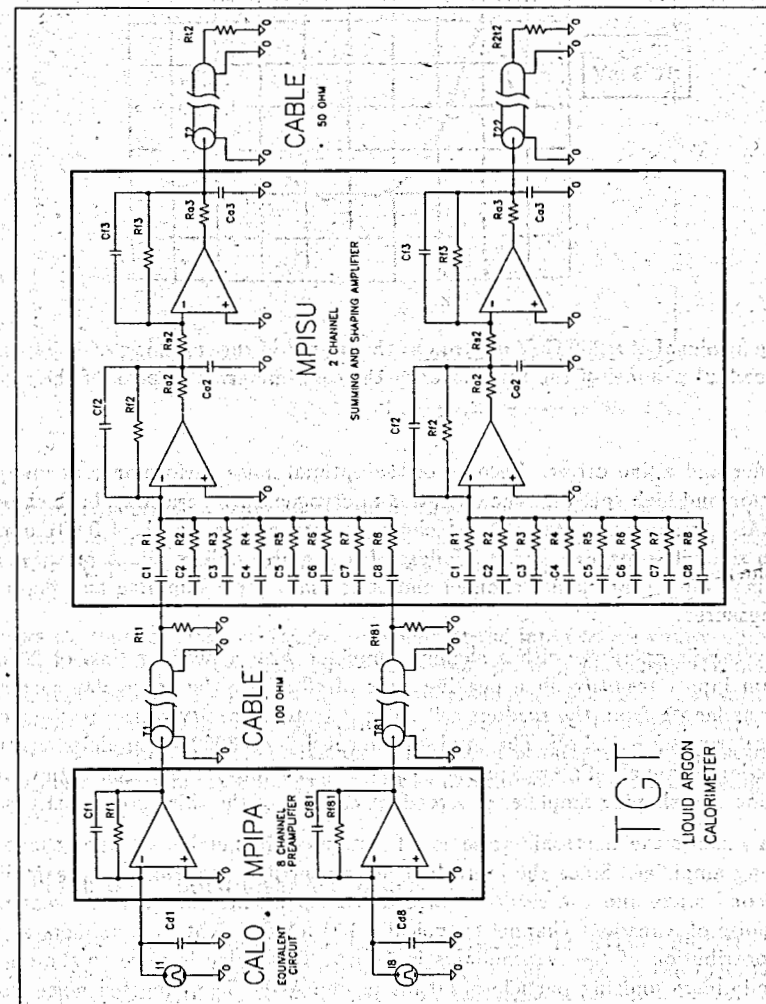

Figure 2: Schematic layout of the front-end electronics of the TGT calorimeter. Both the preamplifiers and the summing and shaping amplifiers are located in the liquid argon close to the detector. The calibration pulsers are located outside of the cryostat in the warm, the calibration input being at the amplifier level.
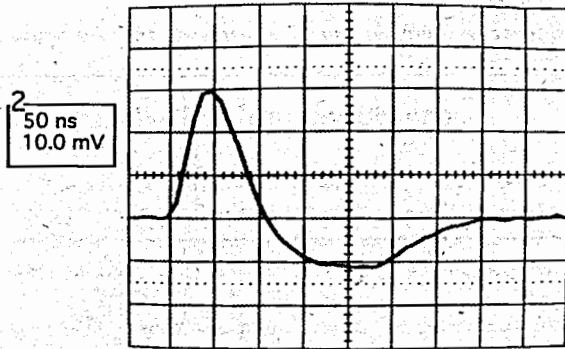
Figure 3: Signal of a 200 GeV electron at the output of the summing and shaping amplifier of a readout channel of the third layer in the calorimeter. The peak of the signal is after 43 ns.

amplifier and a line driver. Because of the optimal noise performance at low power consumption and high speed for the operation at cryogenic temperatures, both chips are made in GaAs technology. A MESFET technology with a gate length of 0.001 mm has been chosen since it is mature, and it is offered by several suppliers [6]. A power consumption of 12 mW for a preamplifier channel and of 150 mW for a summing and shaping channel was measured.

The system is operated with a shaping amplifier with a peaking time of 20 ns for a δ-function input, resulting in a peaking time of 43 ns for the triangular current pulse of ~ 160 ns length from the readout cell. The detector capacity of the readout cells of the TGT calorimeter is 120 pF. The total system consists of 3000 preamplifier channels and of 500 readout channels. Figure 3 displays the signal of a 200 GeV electron at the output of the summing and shaping amplifier of a readout channel of the third layer in the calorimeter.

Figure 4 shows the electronic noise as a function of the number of input channels for the summing amplifier. Since the individual noise contributions from the preamplifier stage, the second stage and the readout stage are independent, they may be separated. The total noise of a readout channel is typically 150 nA for eight preamplifiers at the input. The contribution of the preamplifiers is 51 nA. This value is close to the one expected for a minimum ionizing particle of 60 nA in one ABE. The expected noise from SPICE simulations is 30 nA for the central value in the technological parameter space as guaranteed by the producer. The range of these values may have to be reduced for future fabrication.

In Fig. 5 the distribution of the total electronic noise for a sample of chips after summing eight amplifiers and shaping with a peaking time of 43 ns for a triangular input pulse is shown. Most of the chips show a similar behaviour with a noise of around 140 nA with about 30% of the specimen at higher values. In subsequent mass productions, a selection on the basis of the noise measurement will be made.
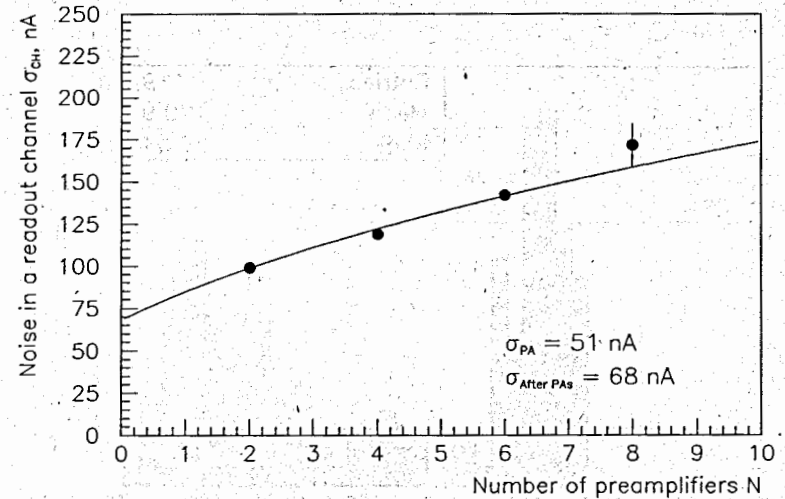

Figure 4: Electronic noise of the summing amplifier as a function of the number of preamplifiers. The noise contribution of a single preamplifier is 51 nA. The noise contribution of the system after the preamplifier is 68 nA which is added in quadrature.

Figure 6 shows the gain variation of the preamplifiers at the input to a common summing stage. Plotted is the deviation of the gain of individual preamplifiers from the mean of the respective eight specimens. This quantity is important since the individual variations can not be calibrated in this specific application. It is observed that the gain variation is well below the $\pm 3\%$ requested. The variation of the signal peaking time for preamplifier channels entering in the same summing channel was determined to be 1.2 ns, being close to the requirement of 1 ns.

3.3 Conclusion on Calorimeter Readout

It was demonstrated that the amplifier electronics developed in RD33 fulfils the LHC requirements for an electromagnetic TGT calorimeter to be operated at the LHC [7]. In addition, irradiation tests with a neutron fluence of 3×10^{14} n/cm^2 and a photonic radiation of 2 Mrad show [8] that a front-end electronic system based on this technology and design can be safely operated for ten years in the radiation conditions of the electromagnetic endcap of ATLAS. Increasing the irradiation up to levels of 6×10^{14} n/cm^2 shows that a limit of a reasonable operation of the amplifiers is approached. On the other hand, during photonic irradiation up to 10 Mrad no changes of the level of electronic noise and only small changes of other observables are measured [8].

Table 2: Energy resolution for MC data using different correction methods (see text). The parameters p_1 and p_2 refer to parameterization $\frac{\sigma(E)}{E} = \sqrt{p_1^2/E + p_2^2}$ (E in GeV).

	p_1	p_2
All channels summed	9.7 ± 0.3	0.6 ± 0.1
Ideal case	10.0 ± 0.4	1.4 ± 0.1
HV lines disconnected	5.1 ± 7.1	6.2 ± 0.2
Average signal correction	13.0 ± 0.9	3.4 ± 0.1
Shower shape correction	12.4 ± 0.6	2.0 ± 0.1
Minimization	13.6 ± 0.4	1.0 ± 0.1

account, yields even better results (solid triangles). Here the signal response of the channel affected by the HV problem relative to the signal distribution of the neighbouring channels has been taken into account via a correction function. This procedure is rather efficient for correcting the HV problems, even though the resolution of the ideal case cannot be restored. Energy leakage is affecting the resolution as well, in particular at higher energies. To take this effect into account, weighting parameters for individual channels have been obtained from a fit minimizing the energy resolution. For this fit all data at different energies and impact points have been used in parallel. As seen in Figs. 7 and 8, the agreement with the ideal case is good, except for a small deviation at low energies.

In order to judge the various contributions to the energy resolution in a more specific way, the energy dependence of the energy resolution has been parameterized by (E in GeV):

$$\frac{\sigma(E)}{E} = \sqrt{p_1^2/E + p_2^2}.$$

The curves in Fig. 7 show the results of these fits to the different data sets. Table 2 shows the energy resolution for the various correction methods applied, for the uncorrected case, the ideal case and the case adding all readout channels of the calorimeter. Given the limited lever arm in energy, the correlation between the sampling term p_1 and the constant term p_2 is by no means negligible. Nevertheless, it is evident that the corrections mainly improve the constant term, finally yielding results which are close to the ideal case.

4.1.2 Energy Resolution and Linearity

A particularly important aspect of the quality of the data is the contribution of the electronic noise to the energy resolution. So far this contribution has not been considered in the MC. The noise has been obtained from random trigger events, adding the signals of those channels used within the reconstruction cone of the electron. A typical value of 480 MeV is obtained from the data. Correcting for disconnected pads by using the expected shower shape, one obtains a value of typically 690 MeV for this noise.

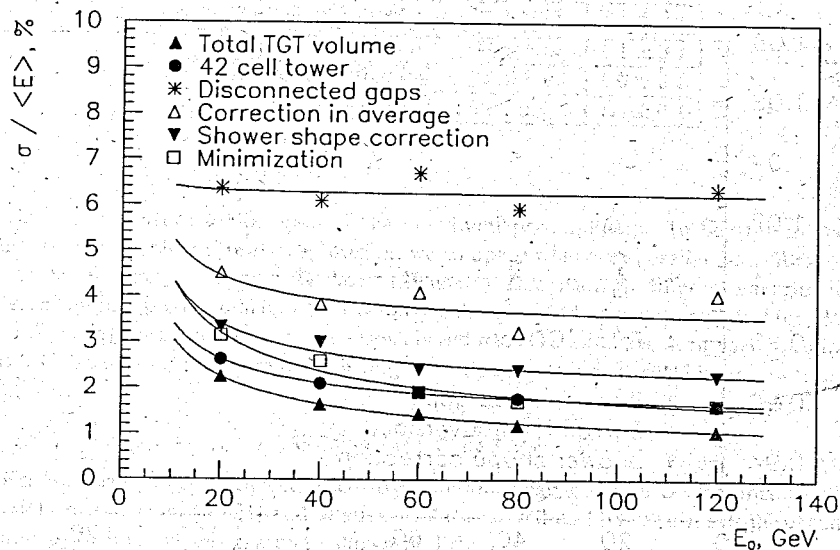A second important aspect is the systematic error related to the calibration procedure,

Figure 7: Energy dependence of the energy resolution σ/E for MC generated electrons. Solid triangles: The energy response of all readout channels has been added. Solid dots: The energy in a restricted volume around the shower axis has been added ('ideal case').
Stars: The gaps which were affected by HV discharge have been disconnected.
Open triangles: The average signal correction has been applied.
Solid inverted triangles: The shower shape correction has been applied.
Open squares: The relative weights of individual channels as obtained from minimizing the energy resolution have been applied.
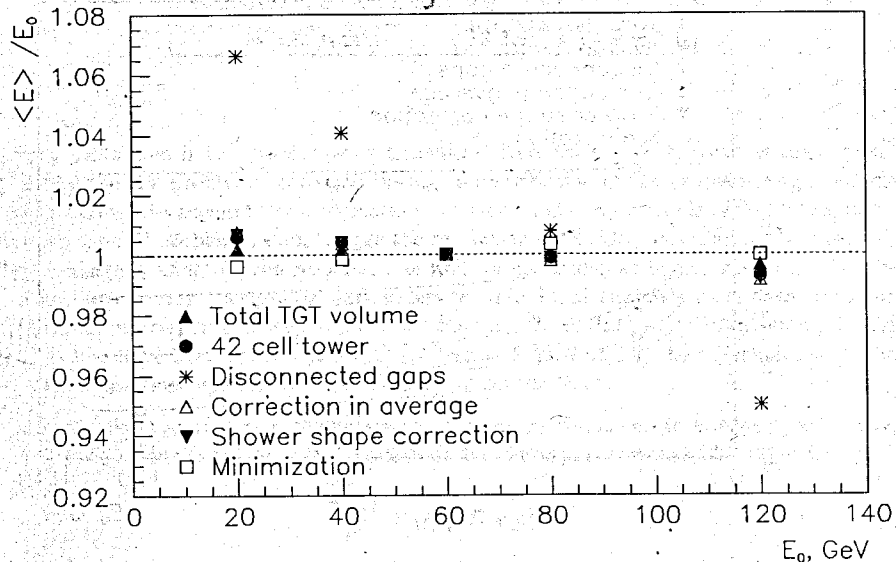The curves represent the results of the respective fits (see text).

Figure 8: Energy dependence of the average energy deposition for MC generated electrons.
Solid triangles: The energy response of all readout channels has been added.
Solid dots: The energy in a restricted volume around the shower axis has been added ('ideal case').
Stars: The gaps which were affected by HV discharge have been disconnected.
Open triangles: The average signal correction has been applied.
Solid inverted triangles: The shower shape correction has been applied.
Open squares: The relative weights of individual channels as obtained from minimizing the energy resolution have been applied.

Table 3: Energy resolution using different correction methods (see text). Given are the parameter p_1 and p_2 using the parameterization $\frac{\sigma(E)}{E} = \sqrt{p_1^2/E + p_2^2 + (p_3/E)^2}$.

MC	p_1	p_2
Shower shape correction	12.2 ± 1.0	2.0 ± 0.1

Data	p_1	p_2
Shower shape correction	9.9 ± 0.6	2.1 ± 0.1
Global minimization	11.8 ± 0.3	1.1 ± 0.1
80 GeV minimization	12.0 ± 0.3	1.0 ± 0.1
MC minimization	11.0 ± 0.6	1.4 ± 0.1

in view of the rather similar gain of the individual preamplifiers. To be able to decouple conclusions from the calibration precision, we compare whenever possible uncalibrated data to the MC prediction. Figure 9a shows the energy resolution at different energies for two different impact points in height for the data (solid dots and open squares) and for MC data (stars). In (a) the shower shape corrections based on MC results has been used both for data and MC. To extract the energy resolution, the following parameterization has been used (E in GeV) :

$$\frac{\sigma(E)}{E} = \sqrt{p_1^2/E + p_2^2 + (p_3/E)^2}.$$

The noise term p_3 has been extracted from random trigger events as described above (i.e. not determined from the fit) and applied to data as well as MC. The resulting parameters p_1 and p_2 for the various cases are shown in Tab. 3.

The fit of the data yields a sampling term $p_1 = 9.9 \pm 0.6\%$ and a constant term $p_2 = 2.1 \pm 0.1\%$. The corresponding numbers for the MC data are $p_1 = 12.2 \pm 1.0\%$ and $p_2 = 2.0 \pm 0.1\%$. The agreement is rather good, in particular in view of the fact that no calibration has been used for the data. In a next step weighting parameters for individual channels have been obtained from a global fit to all available data (all energies and impact points). This improves the energy resolution of the data not only because energy leakage is corrected to a certain level, but also because effective calibration corrections are determined for the individual readout channels as well. The impact of this method on the energy resolution is demonstrated in Fig. 9b. For the data the fit yields a sampling term $p_1 = 11.8 \pm 0.3\%$ and a constant term $p_2 = 1.1 \pm 0.1\%$. Solely using the 80 GeV data in the minimization (Fig. 9c), the corresponding numbers are $p_1 = 12.0 \pm 0.3\%$ and $p_2 = 1.0 \pm 0.1\%$. Within errors the results are identical. Using weighting parameters obtained from MC and applying them to the data yields the result shown in Fig. 9d. One obtains a sampling term $p_1 = 11.0 \pm 0.6\%$ and a constant term $p_2 = 1.4 \pm 0.1\%$. These values compare rather well with case (b) and show that the impact of the precision of the calibration of the individual channels on the energy resolution does not exceed the impact of energy leakage, as visible in the constant term p_2.
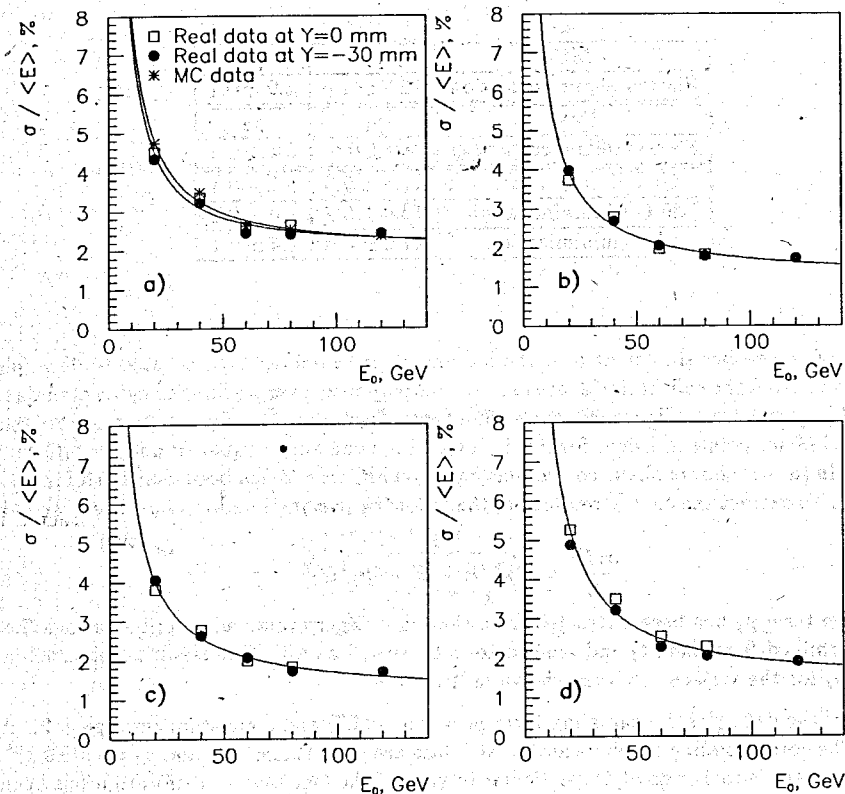
Figure 9: Energy dependence of the energy resolution σ/E for the data at two different impact points in y (solid dots and open squares) and the corresponding MC prediction (stars). The solid curve shows the result of a three parameter fit (see text). Different correction procedures have been applied to both data and MC:
a: shower shape correction based on MC results,
b: weighting parameters for individual readout channels from a global fit,
c: weighting parameters as obtained when solely using the data at 80 GeV in the fit,
d: weighting parameters as obtained from MC events and applied to the data.

The linearity of the energy response has been studied in Fig. 10. Shown is the response using the shower shape correction (Fig. 10a), applying the minimization method in a global fit (Fig. 10b), and in a fit to the 80 GeV data only (Fig. 10c) and in a global fit to all MC data. The nonlinearity, as shown in Fig. 10a, is typically at the level of ±1.5% for the data and ±1% for the MC prediction. We attribute the difference to the fact that the data are uncalibrated. Applying for the data weighting parameters of individual channels (Fig. 10b and Fig. 10c) improves the linearity substantially, as expected. But using the corresponding weighting parameters from MC events (Fig. 10d), essentially yields the same result. This shows again that the weighting parameters compensate to some extent the energy leakage in the MC. But for the data these parameters compensate for both effects, energy leakage and mis-calibration of individual readout channels in the data.

4.1.3 Angular Resolution

One of the important questions related to the performance of an electromagnetic calorimeter is the resolution of the reconstruction of the angle of an incident photon. We studied the angular resolution using electron data at different energies, in particular in the region equipped with horizontal and vertical strips (Fig. 1). Using the information of the high resolution proportional chambers in the beam line, the impact direction of each individual beam particle is known to high precision. This impact direction can directly be compared with the reconstructed shower axis using the fine longitudinal and lateral segmentation of the calorimeter. The barycentre of the electromagnetic shower has been reconstructed in each quasi-longitudinal layer, using the geometrical information and energy distribution of the related channels. Depending on the impact point relative to the readout cell centre, this measurement is subject to systematic shifts. To correct for these shifts, Monte Carlo events with energy and impact point distributions identical to the real beam particles have been generated. The correction function, obtained from these Monte Carlo events, has been parameterized using a third order polynomial function.

Figure 11 shows the energy dependence of the angular resolution σ_θ[mrad] of reconstructed electron showers for the two options using the strip information (open points) or ignoring this information (solid points) for data (Fig. 11a) and simulated events (Fig. 11b). The curves are a fit using a parameterization $\sigma_\theta = \sqrt{a^2/E + b^2}$. Table 4 shows the parameters a and b obtained for the data and Monte Carlo for both cases, ignoring or using the strip information.

The agreement between data and Monte Carlo is rather good, although a and b show some difference due to the residual correlation. To evaluate the effect of the strips in a more transparent way, in particular to avoid the correlation between a and b, a simple $1/\sqrt{E}$ fit to the angular resolution has been carried out as well. This parameterization fits the data only marginally worse. Taking the mean value within the energy range, we obtain for the data $\sigma_\theta \times \sqrt{E} = 51.8$ [mrad $\times \sqrt{\text{GeV}}$] for the case where the strip information is ignored, and $\sigma_\theta \times \sqrt{E} = 40.9$ [mrad $\times \sqrt{\text{GeV}}$] for the case where the strip information is used. The corresponding values for the MC prediction are 49.2 [mrad $\times \sqrt{\text{GeV}}$] and 38.4 [mrad $\times \sqrt{\text{GeV}}$] respectively. For both options the agreement between data and Monte Carlo is rather good, the Monte Carlo showing a resolution being slightly better by $\sim$ 5%).
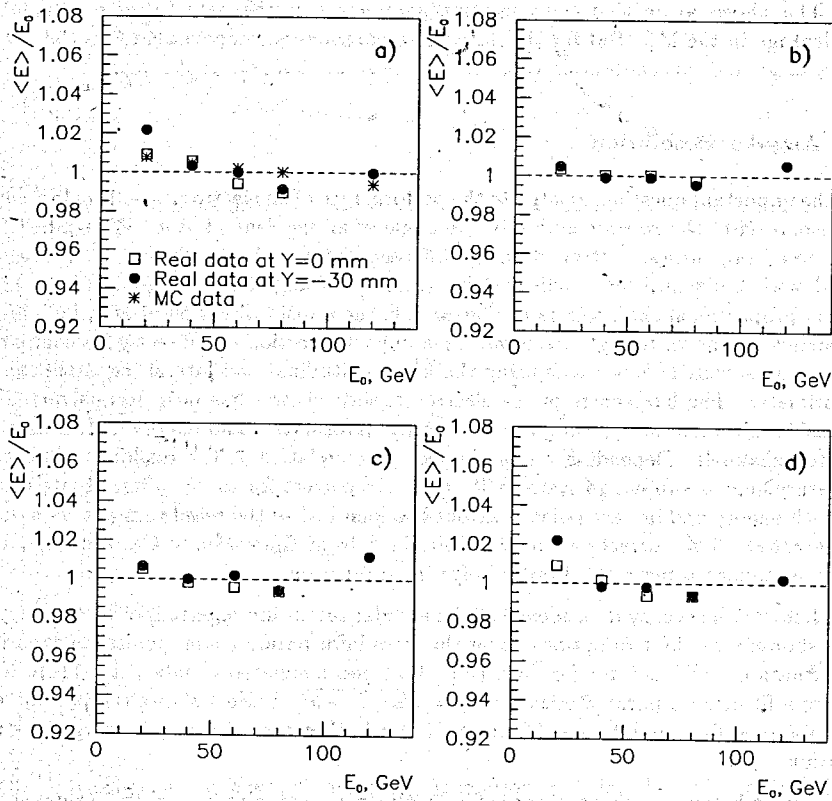
Figure 10: Energy dependence of the energy response for electrons. Shown is the response using the shower shape correction (a), using the minimization method in a global fit (b), in a fit to the 80 GeV data only (c) and in a global fit to all MC data (d).
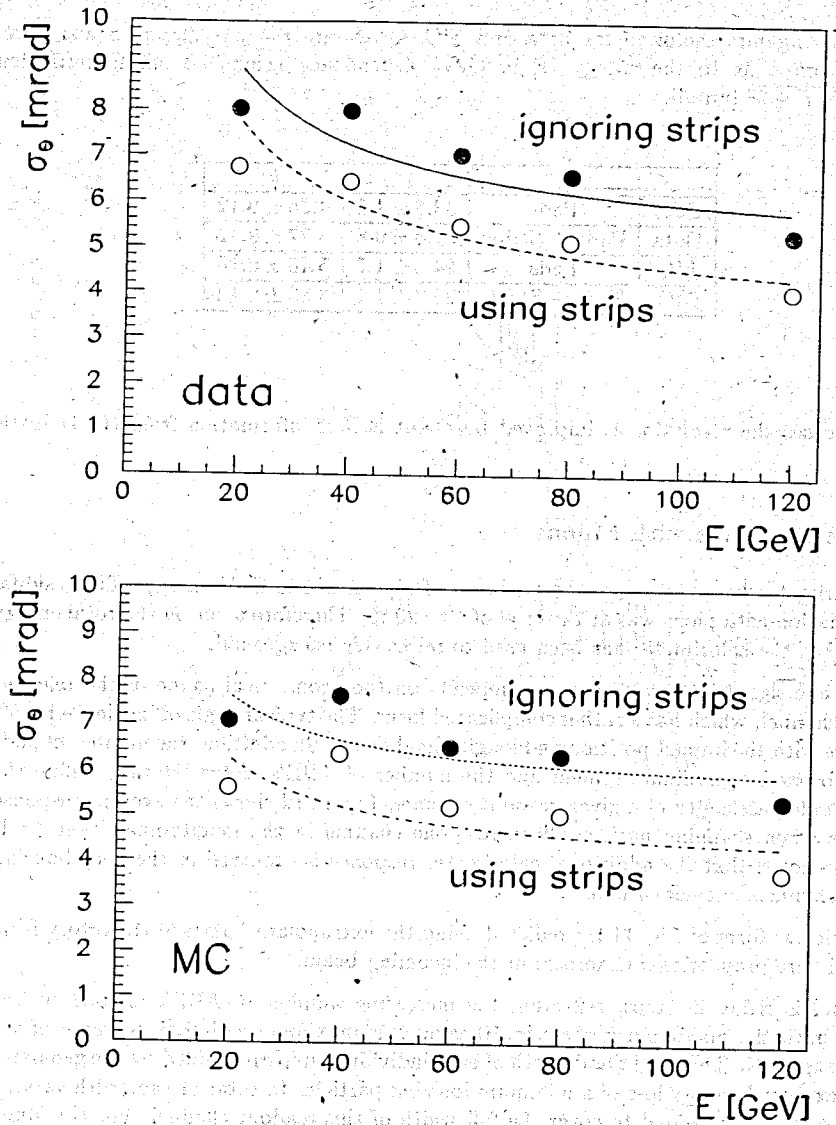

Figure 11: Energy dependence of the angular resolution σ_θ[mrad] of reconstructed electron showers for the two options using the strip information (open circles) or ignoring this information (solid circles) for data (a) and MC (b). The curves shown are a fit using a parameterization $\sigma_\theta = \sqrt{a^2/E + b^2}$.

Table 4: Angular resolution for data and MC. Given are the parameters a and b resulting from a fit to the energy (E in GeV) dependence using the parameterization $\sigma_\theta = \sqrt{a^2/E + b^2}$ [mrad].

		a	b
Data	Pads	33.6 ± 1.0	4.95 ± 0.12
Data	Pads + Strips	31.8 ± 0.8	3.27 ± 0.12
MC	Pads	24.0 ± 1.7	5.46 ± 0.16
MC	Pads + Strips	22.2 ± 1.1	3.85 ± 0.13

In both cases the resolution is improved by about 20% if information from the strips is used.

4.2 Performance with Muons

The calorimeter has been exposed to a beam of muons of 120 GeV energy. The residual contamination with pions was at the level of 10 – 20 %. Therefore a cut on the total energy deposited in the calorimeter has been used to reject this background.

The average signal response to muons depends on the geometrical shape of the relevant readout channel, which has a rather complicated form. The typical angle of incidence is 45°, but varies with the impact position and longitudinal depth. In addition, the number of pads ganged to one longitudinal segment and the number of ABE's added laterally define the total particle passlength of a given readout channel. Figure 12 shows the average response of muons when scanning horizontally across one channel in the longitudinal layer 4. It should be noted that the additional calorimeter response is observed in the neighbouring readout channels not added here.

The particular form of Fig. 11 is predicted using the extrapolated particle trajectory from the multi wire proportional chambers in the incoming beam.

The signal is rising in steps, reflecting the increasing number of ABE's crossed by the particle, until the maximum is reached. Beyond this maximum a similar decrease of the signal is expected. The height and width of each individual step are defined by the geometry and the expected energy loss of a minimum ionizing particle. In total 11 runs with varying impact positions are added to cover the full width of this readout channel. For the muon data the HV correction used is a simple factor corresponding to the ratio between active gaps and HV disconnected gaps per readout channel. The fit (solid curve) yields a muon response of 50.5 ± 1.5 nA per ABE. From a comparison to the absolute prediction we derive an e/μ ratio of 1.2, compatible with expectations.
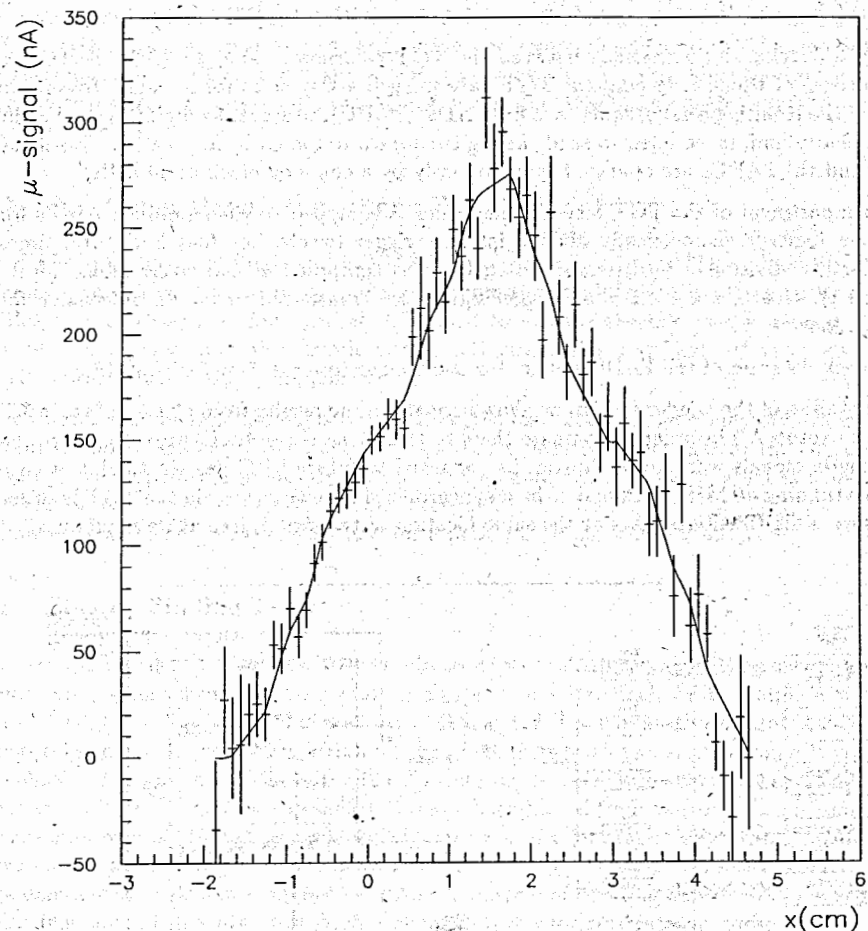

Figure 12: Average muon signal (nA) when scanning across a readout channel in the longitudinal layer 4. The solid line is a fit to the data, based on the expected passlength variation due to the particular geometry of this channel.

5 The Calorimeter Trigger System – The Hardware

In the LHC experiments, the electromagnetic calorimeter will be used to provide a powerful level-1 trigger for electrons. The RD27 collaboration [3] has developed methods, algorithms and also hardware for this purpose. In particular, a so called 'Cluster Finding Module' (CFM) [4] was built and operated also in connection with the TGT calorimeter.

We have developed an interface between the TGT calorimeter and the CFM electronics the purpose of which is to combine TGT data in such a way as to form trigger towers, to digitize the resulting analog sums by a flash ADC (FADC), to store the digital pulse-height in a memory and, in parallel, to send the digitized data to the CFM for analysis. Both the CFM and the FADCs are operated synchronously by a common clock at 40 MHz.

The compartment of the TGT test-module, which is equipped to yield summed signals for a trigger logic, is geometrically divided into 16 trigger towers, i.e. four horizontal times four vertical divisions. Furthermore, each tower is composed of five layers along depth. (Figure 1). Hence, $4 \times 4 \times 5 = 80$ trigger signals are transferred to the FADC-system for digitization.

The block diagram of the FADC system for one trigger tower is shown in Fig. 13.

As for studies of the trigger system we show here also some results from phase I of the TGT project ('setup A') in order to compare them to the phase II results ('setup B') where the calorimeter signals were much shorter, i.e. adapted to future LHC use. In the latter case the free running 40 MHz clock had to be resynchronized for every event in the TGT in order to ensure a digitization always at the same location of the signal, e.g. at its maximum.
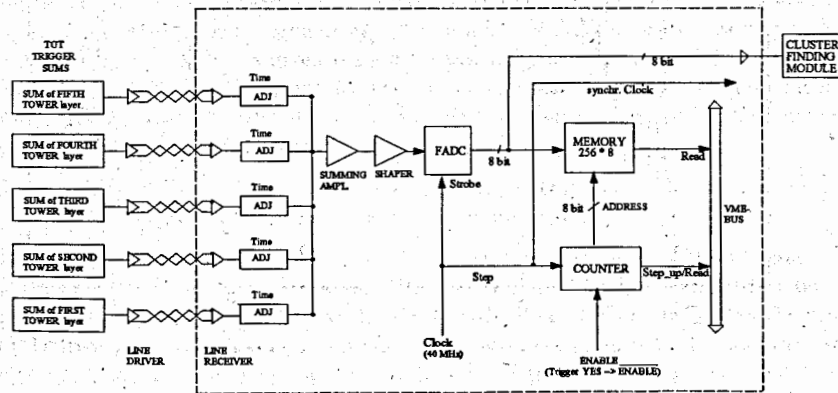

Figure 13: Block diagram of the FADC-module. Signals are received from the calorimeter, summed to form trigger towers and shaped before being digitized. The digitized data are fed into the cluster finding module for further processing.

5.1 The Trigger Signals from the TGT Test-Module

Signals from the preamplifiers arrive via cables ($\sim$ 60 m in setup A, 4 m in setup B) at a patch-panel, where they are reordered to connect to the FADC system. This system consists of 8 modules being housed in one VME-crate. A free-running 40 MHz clock is generated in the 'Cluster Finding Module' and fanned out to the 8 FADC-boards. The 'YES'-decision is used to stop ADC-conversion and freeze the memories. The two output bytes from each FADC-board - along with the clock signal for re-synchronisation - are directly transferred to interfaces in the CFM, where the ASIC-based logic of RD27 derives a trigger decision.

5.2 Functional Description of one FADC-Module

An FADC-module is a single-width VME-board containing two FADC-channels. Each channel receives five twisted-pair input signals from the depth-layers of a trigger tower. An analog sum of these five input signals is formed to provide the full energy deposit. The output signal is reshaped in a hybrid-circuit (H1 design [5]) and digitized via a 40 MHz FADC (LHC bunch crossing frequency).

In addition, each FADC-channel is equipped with a fast, 256 byte long memory, where the output is stored. On every clock cycle the address is increased and reset at the end of the memory. This operating mode provides a 'circular data buffer'. The content is frozen by a 'YES'-decision from the CFM. It can subsequently be readout via the VME-bus. The memory shows the digitization 'history' for a period of 25 ns $\times$ 256 = 6.4 μs.

5.3 Cluster Finding Logic

The trigger system (CFM) executes an electron/photon trigger algorithm using ASICs which process digital calorimeter signals at a rate of 40 MHz. Each ASIC computes within a 4×4 trigger cell window the energies of 2×1 and 1×2 cells (horizontal $\times$ vertical signal cells) of the inner 2×2 matrix and compares them with two electromagnetic cluster thresholds. The energies of the outer 12 cells (referred to as isolation ring) are summed and compared with two isolation thresholds to reject background from hadrons. In addition the energy sum over all 16 cells is provided for later use in a jet trigger algorithm. The 4×4 windows are overlapping and shifted by units of one trigger cell with respect to each other. The demonstrator system contains 3×3 ASICs capable of covering an area of 6×6 trigger cells. It is housed in a nine inch high crate with a bus for readout and control interfaced to VME. Details can be found in [4].

5.4 Re-synchronisation of the FADC Clock

In order to simulate the conditions at LHC, where one has a fixed time relation between the LHC clock and the calorimeter signal, the 40 MHz clock was re-synchronized to single incoming beam particles. This was achieved by using an early scintillator pickup signal from the beam (Fig. 14) which arrived several clock cycles before the calorimeter signal at

the FADC input. The same fast signal was also used to synchronize the digitization and readout sequence of the TGT calorimeter proper.
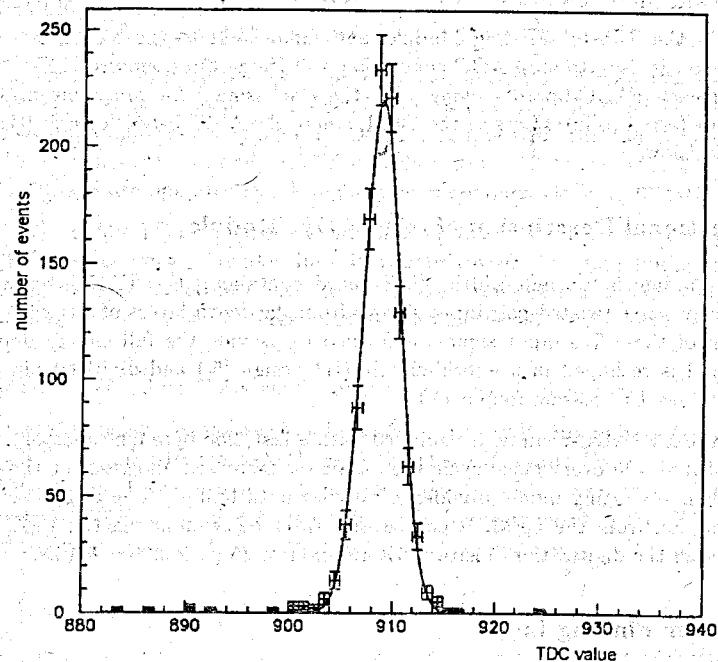

Figure 14: Time distribution of the fast beam trigger signal from two small scintillation counters in coincidence measured with a TDC (25 ps per count). The time resolution is about 70 ps. The actual signal shown is obtained by convoluting the seperate signals of the two counters.

6   Performance of the Trigger in the Test Beam

A 4 × 4 trigger cell window was implemented with transverse dimensions of a basic trigger cell of 4.8 × 6.0 cm² in setup A and of 9.0 × 9.0 cm² in setup B. The trigger system including the FADCs was controled and readout by a standalone data acquisition system using a MacIntosh computer with a MICRON/MacVEE interface to VME in setup A and by a combined OS9 readout system in setup B. It was triggered by a beam signal derived from scintillation counters (2 cm × 2 cm) and a DISC Cerenkov counter yielding well defined signals of electrons or hadrons. The following data were recorded: 16 × 8 bit FADC

data, 36 × 8 bit data from the input memories of the trigger system, 9 × 12 bit energy sums over the trigger cell windows covered by the CFM and 9 × 2 'hit' bits from the trigger algorithm for the two sets of thresholds. For each event this information is sampled 255 times at 25 ns intervals. To limit the event size, usually only 50 samples were readout giving an event size of 3.5 kbytes.

6.1   FADC Response to Calorimeter Signals

Electron, muon and pion beams of different energies (electrons of 20, 40, 60, 80, 120, 200 GeV, muons of 120 GeV and pions of 200 GeV) and different impact positions on the calorimeter are used to analyze the behaviour of the trigger system. As an example in Fig. 15 the shaped and digitized data of a typical electron event at 80 GeV are shown, both with a slow shaper (setup A, $\tau \approx 100$ ns) and with a fast shaper (setup B, $\tau \approx 12$ ns). The energy deposit in the isolation ring is indicated by the shaded area.

When analyzing the recorded data, we proceed in the following way: First the FADC output values are used to extract general features of the calorimeter trigger. In the next step this output is compared to the CFM input memory which should be just a copy of the FADC output. Ensuring that both systems do handle the same event, the CFM outputs - namely the energy sum and the hit pattern - are studied.

6.2   Analysis of FADC Data

The FADC output data are used to study shower containment of electromagnetic and hadronic showers, noise, the threshold behaviour of the trigger system and to simulate the response of the CFM for different trigger algorithms. In setup A the trigger cell size during these tests was smaller than the finally envisaged cell structure. This allows detailed study of the shower profile with respect to trigger granularity. However, the study of the isolation criterium is limited because only 16 basic cells could be instrumented. In setup B the final trigger cell size was adopted. In a first study the energy response of the trigger system has been compared to the calorimeter readout stream. Pions were selected in order to cover a large energy range. In Fig. 16 such events entering the calorimeter at different beam impact points are shown: despite the fact that the data are uncalibrated and stem from different regions of the calorimeter, a good correlation between the energy seen by the FADC readout and the energy seen directly in the calorimeter is observed. In Fig. 17 the mean value of the energy response is shown as a function of the electron beam energy. The response is linear up to highest energies available in the test beam. Moreover it seems that the 2 × 1 cell configuration is sufficient to contain electromagnetic showers almost completely. The calibration constant is calculated to 0.87 FADC counts per GeV. The study allows to determine the resolution at each energy point (Tab. 5).

The FADC output data are used to study the response of the CFM for various trigger cell sizes and to study the containment of electromagnetic and hadronic showers in the TGT module. In particular the resolution has been studied for different lateral sizes of a trigger tower by combining basic cells, i.e. by merging signals from 2, 4, 9 and 16 cells (Fig. 18). The nominal cell size foreseen for LHC yields the best result in terms of resolution.
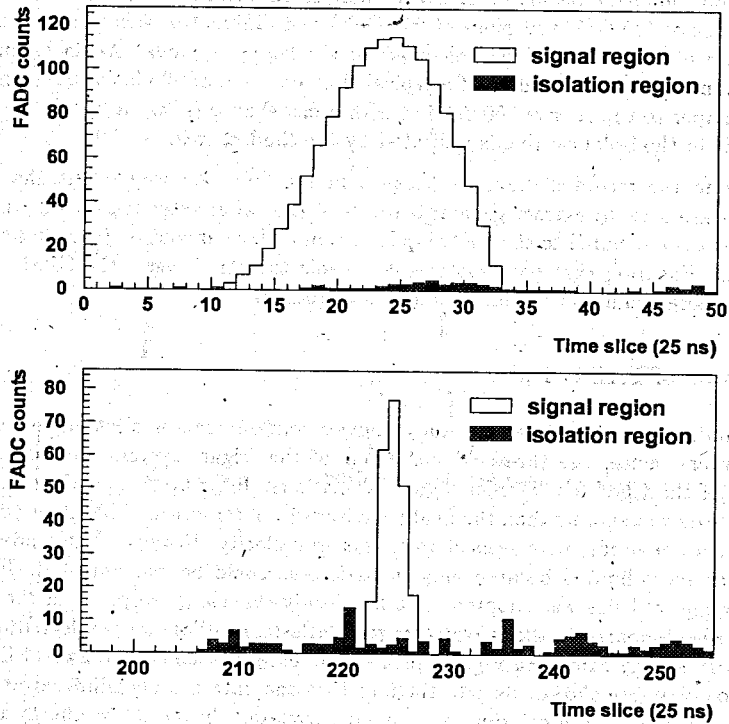
Figure 15: Energy in the signal region and energy in the isolation ring for a single electron as a function of time. The upper figure is for a slow signal with a shaping time $\tau \approx 100$ ns ('setup A'), the lower for a fast one with a shaping time $\tau \approx 12$ ns ('setup B'). The FADC digitization is stopped by a positive decision of the CFM.
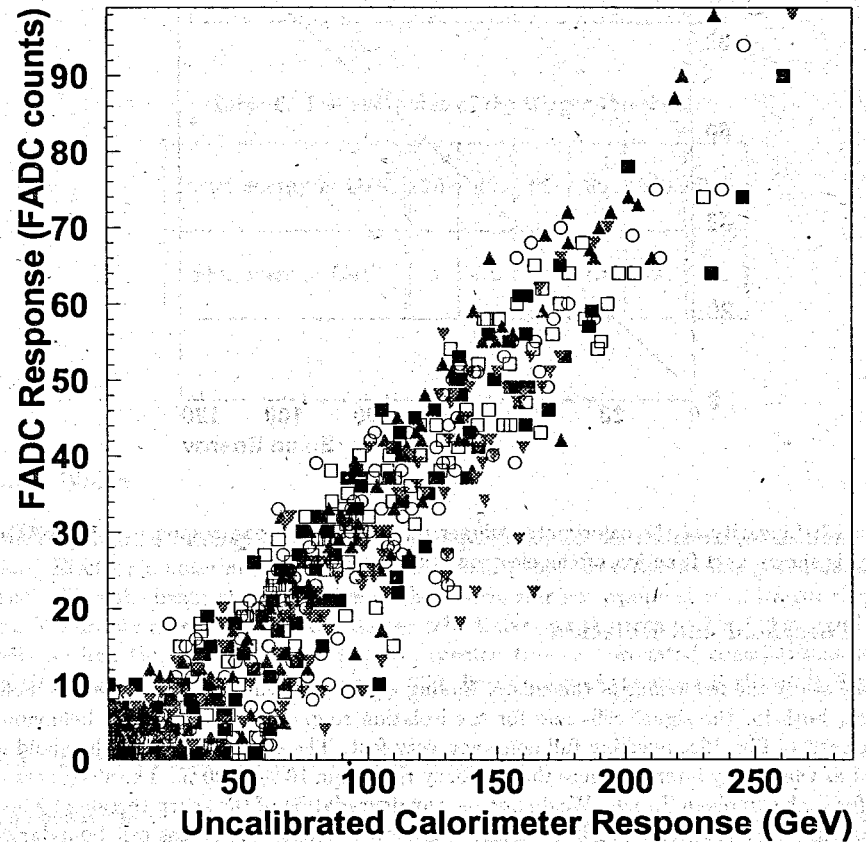

Figure 16: The correlation between the energy seen by the FADC system and the energy measured in the calorimeter.
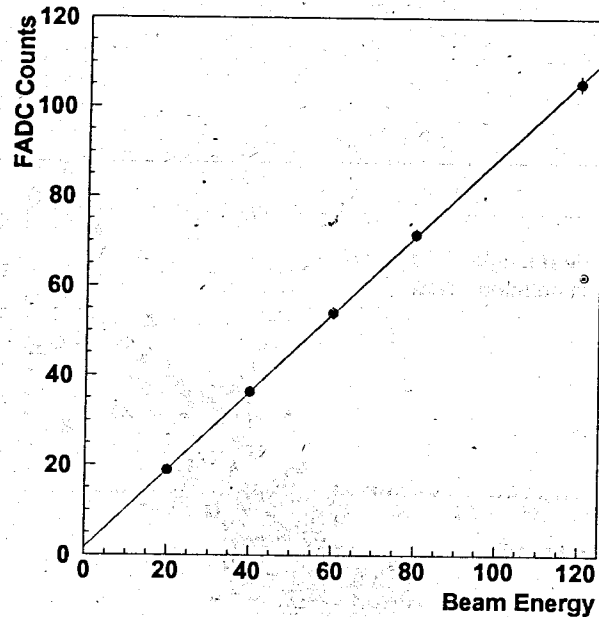
Figure 17: Linearity of the calorimeter trigger readout: The mean response of the FADC system is shown as a function of the electron beam energy.

6.3   Threshold and Isolation

Next we study the behaviour of the cluster finding algorithm as a function of the threshold settings, both for the signal cells and for the isolation ring. A sharp threshold behaviour can be seen in Fig. 19a, reaching full efficiency very fast. The sharpness of the threshold is defined as the energy interval where the efficiency rises from 10 % to 90 %. The sharpness is given for each sample in Tab. 6. We do not see any degradation of the sharp threshold when varying the center of the beam impact although no detailed scans across cell boundaries were performed. In Fig. 19b the second condition, i.e. isolation, of the CFM is illustrated. Plotted is the fraction of electrons/pions as a function of energy deposit in the isolation ring (in FADC counts). As can be seen, already at energies around 7 GeV only a small fraction of electrons is rejected (5%) which indicates again that the shower is well contained in the signal region and additional energy spreading out into the isolation ring is small. The fraction of pions which will be rejected at this isolation threshold is 90%. Note that the trigger logic of the CFM requires both trigger conditions studied in Fig. 19 to be fulfilled. We conclude that an isolation threshold of only a few counts is needed in order to reject hadronic showers with high efficiency.

Table 5: Energy resolution obtained with the FADC system.

Beam energy in GeV	20	40	60	80	120
Resolution σ in GeV	2.5	3.1	4.6	4.7	6.3

Table 6: The sharpness of the trigger threshold.

Beam energy in GeV	20	40	60	80	120	200
Sharpness in GeV	3	4.5	5.5	7.5	9	15

6.4   Noise

Not only remnant energy in the isolation ring determines the threshold for hadrons rejection. Electronic noise must be taken into account, too. To estimate this noise, data were used where the beam enters a region of the calorimeter not equipped with trigger electronics. We obtain a figure of 0.55 counts per cell. Enlarging the area to 2 × 2, 3 × 3 and 4 × 4 cells we find that the noise increases as expected from uncorrelated contributions with a small contribution from coherent noise. The distribution of the noise is shown in Fig. 20.

6.5   Response of the Cluster Finding Logic

The behaviour of the cluster finding logic can be tested by repeating its operation off-line, using its digitized input as stored and subsequently readout in the FADC system.

In order to correlate the CFM input to the output the FADC data are used to calculate an expected bit pattern as a function of time. This pattern is then compared to the bitpattern output of the CFM module. Both systems yielded results in perfect agreement: not a single event was lost by the CFM nor any event accepted wrongly as can be seen in the Fig. 21. However, in a fraction (20 per cent) of the events, the ASIC seems to get out of beat: the trigger hit pattern and the digital input were out of step by one time bucket of 25 ns.
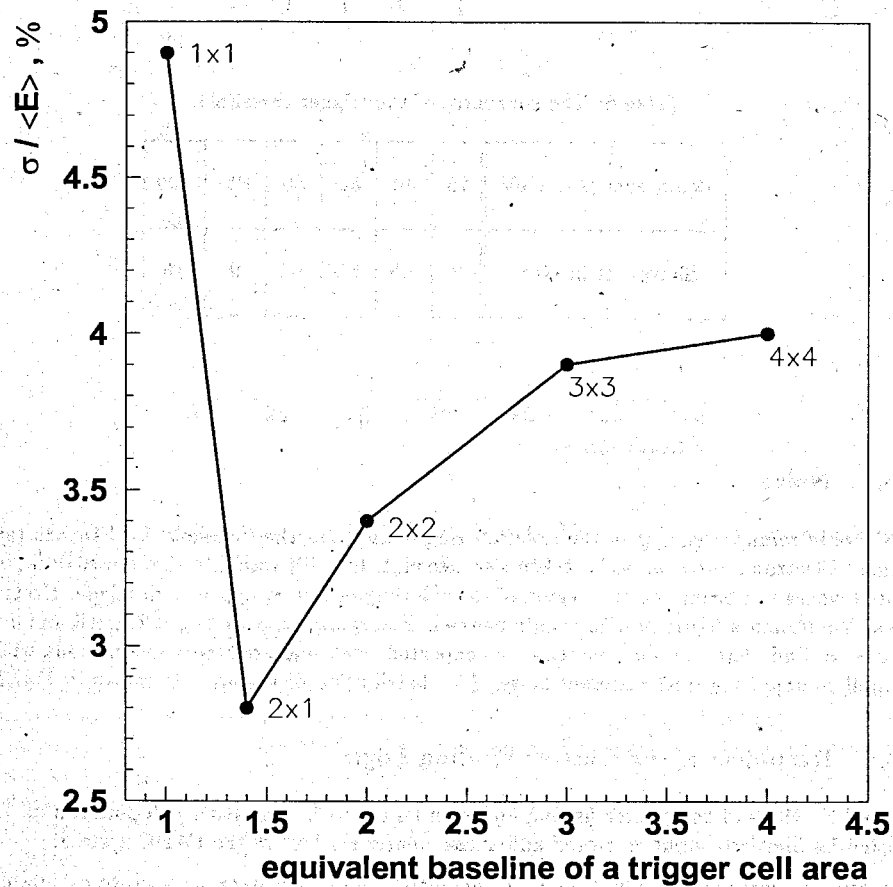
Figure 18: The trigger efficiency and the trigger as a function of the trigger cell size. With the nominal cell size of 2×1 an optimum resolution is reached.
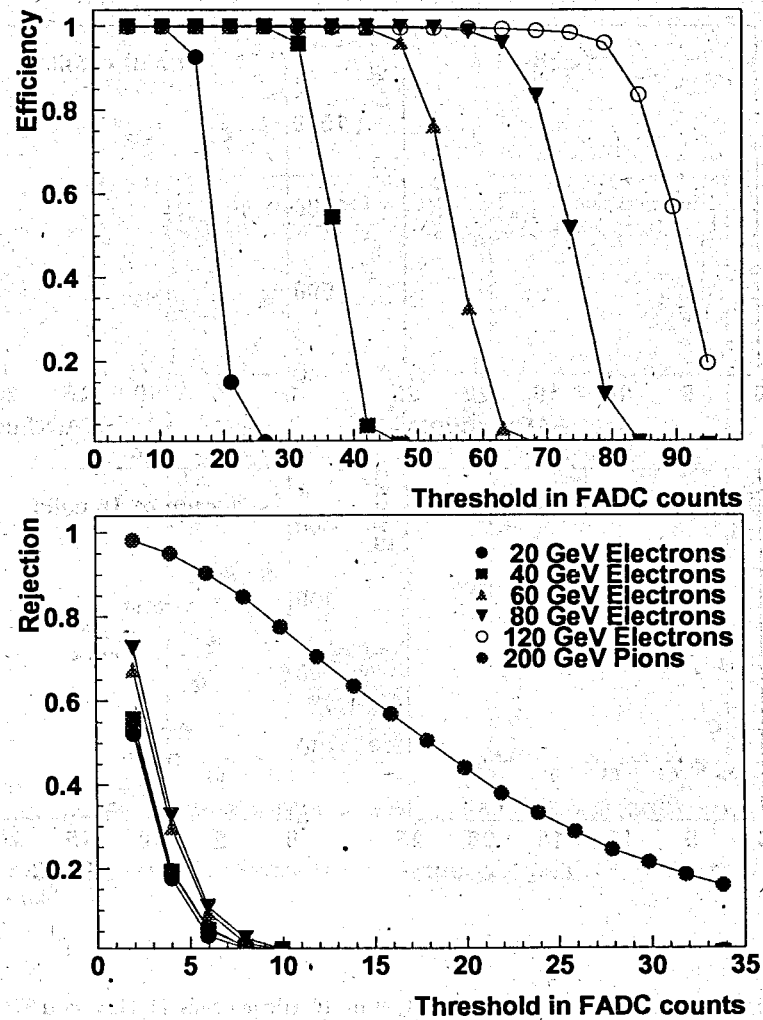

Figure 19: (a) Trigger efficiency as a function of the signal threshold (no isolation requirement) (b) efficiency of the isolation threshold.
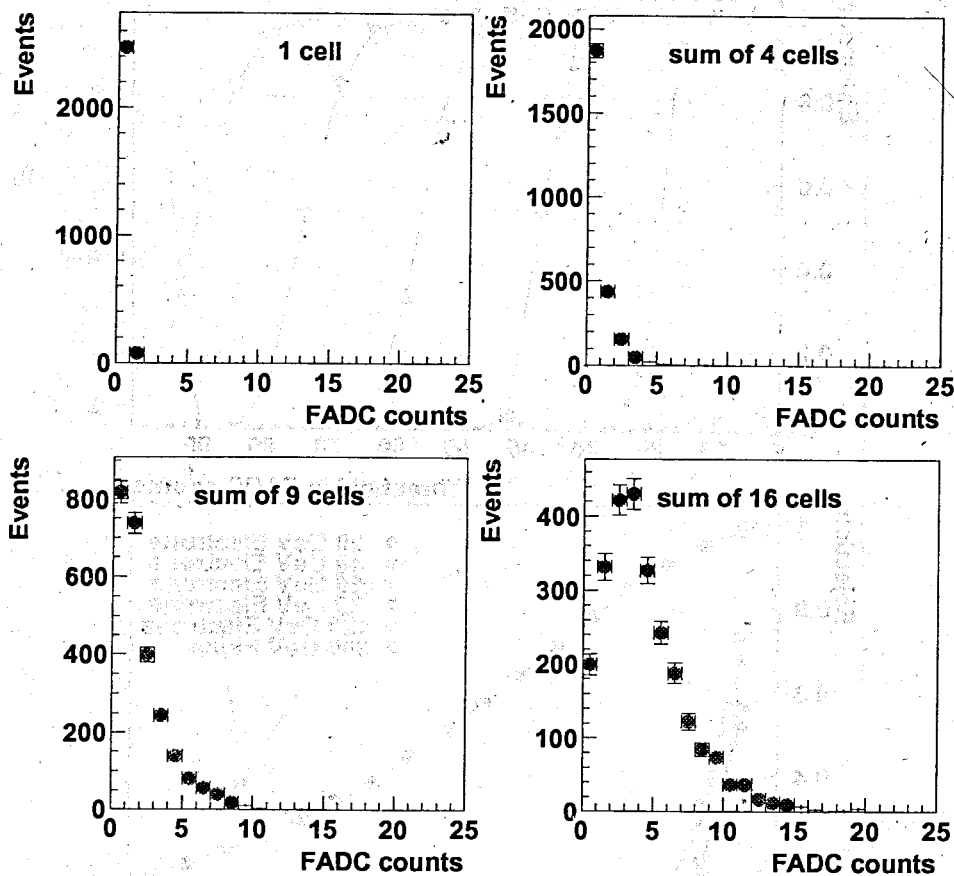
Figure 20: Noise (in FADC counts) in 1, 4, 9 or 16 trigger cells (1 GeV is 0.87 FADC counts).
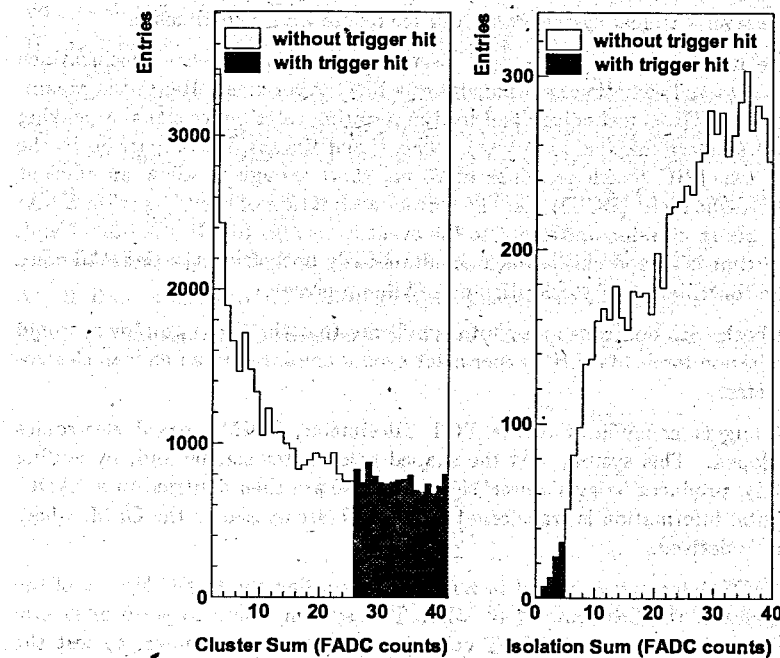

Figure 21: (a) Left side: Events (no isolation requirement) (b) efficiency of the isolation threshold.

7 Conclusion

A novel concept of a LAr calorimeter, the TGT, for use at high energy, high rate accelerators, like the LHC, has been developed and a test module has been built and operated in a particle beam.

A detailed description of the technical design and results from phase I of its operation have already been given in [1].

The main emphasis of phase II of the project described here was the test of new cold (i.e. placed in the LAr) front-end electronics and of the ability of the TGT to be used in connection with a level-1 trigger system conceived for future LHC experiments.

In particular, the newly developed front-end electronics had to fulfil the specifications dictated by event rate and radiation environment of a LHC experiment. Hence the preamplifiers were realized in GaAs technology and for the resulting calorimeter signal a peaking time of around 40 ns after shaping was chosen. This signal time is, in comparison to the distance between two LHC bunch crossings of 25 ns, short enough to allow an efficient 'bunch crossing identification' (BCID), i.e. the correct attribution of every signal in a LAr calorimeter to its bunch crossing and hence to the event it belongs to. On the other hand, the 40 ns peaking time is a good choice when simultaneously optimizing the signal to noise ratio both for the contribution of stochastic and of pile-up noise.

Irradiation tests both with neutrons and photons indicate that the GaAs amplifiers would withstand the radiation levels of a LHC experiment even if employed in an endcap electromagnetic calorimeter.

In order to test trigger capabilities of the TGT calorimeter, a VME based electronics system was developed. This system uses the shaped calorimeter signals and, by adding them appropriately, produces 'trigger tower' signals. These are then digitized in a FADC. The resulting digital information is transferred to a BCID circuit and to the CFM, where a trigger decision is derived.

In parallel, the FADC information is kept in a memory recording the FADC history of the past 256 clock cycles at the LHC rate of 40 MHz. This system allows to perform several tasks: to test the performance of the TGT calorimeter for trigger purposes; to test the failure rate both of the BCID and of the CFM electronics by replaying the FADC data offline, to test the agreement between the summed information of trigger towers and the one readout directly in the normal TGT data stream.

We obtain the following results: Although the information in the trigger stream comes from the raw, uncalibrated data, a sharp threshold behaviour is observed in the trigger response. The energy resolution of the trigger signal is adequate for the purposes of future LHC experiments.

As for the trigger circuitery proper, we find, by replaying the data, that both the BCID and the CFM logic make 100 % correct decisions.

The FADC system and its readable memory developed in the context of this project, are a powerful diagnostic tool for the performance both of the calorimeter and the trigger logic.

References

[1] RD33 Collaboration, Ch. Berger et al., Proposal CERN/DRDC 93-02 (1993).

[2] RD33 Collaboration, Ch. Berger et al., Study of a Novel Electromagnetic Liquid Argon Calorimeter - the TGT, NIM A357 (1995), 333.

[3] I.P. Brawn et al., RD27 status report, CERN-DRDC/93-32, RD27 note 22.

[4] I.P. Brawn et al., NIM A349 (1994) 356.

[5] H1 Calorimeter Group, The H1 Liquid Argon Calorimeter System, NIM A336 (1993), 460.

[6] TRIQUINT QED/A process.

[7] H. Oberlack, Cold GaAs Front-end System for the Liquid Argon Hadronic Endcap Calorimeter of ATLAS,
Proceedings of First Workshop on Electronics for LHC Experiments, Lisbon (1995), 253.

[8] J. Ban et al., Radiation Hardness Tests of GaAs Amplifiers for Liquid Argon Calorimetry, JINR Dubna E13-95-222 and MPI München report MPI-PhE/95-08 (1995).

[9] H. Brettel et al., The GaAs Front-end Electronics of the TGT Calorimeter. (1996) (to be submitted to NIM A.)

[10] ATLAS Technical Proposal, CERN/LHCC/94-43, LHCC/P2 (1994).

[11] R. Brun et al., GEANT3, CERN Program Library Writeup W5013.

[12] H.U. Bengtsson and T. Sjostrand, PYTHIA, Comput. Phys. Comm. 46 (1987) 43.